Morphological transitions of elastic filaments in shear flow

Yanan Liu[a,1], Brato Chakrabarti[b,1], David Saintillan[b], Anke Lindner[a,2], and Olivia du Roure[a]

[a]Physique et Mécanique des Milieux Hétérogènes (PMMH), ESPCI Paris, PSL University, CNRS, Sorbonne Université, Université Paris Diderot, 75005 Paris, France; and [b]Department of Mechanical and Aerospace Engineering, University of California San Diego, La Jolla, CA 92093

Edited by Howard A. Stone, Princeton University, Princeton, NJ, and approved August 3, 2018 (received for review March 31, 2018)

The morphological dynamics, instabilities, and transitions of elastic filaments in viscous flows underlie a wealth of biophysical processes from flagellar propulsion to intracellular streaming and are also key to deciphering the rheological behavior of many complex fluids and soft materials. Here, we combine experiments and computational modeling to elucidate the dynamical regimes and morphological transitions of elastic Brownian filaments in a simple shear flow. Actin filaments are used as an experimental model system and their conformations are investigated through fluorescence microscopy in microfluidic channels. Simulations matching the experimental conditions are also performed using inextensible Euler–Bernoulli beam theory and nonlocal slender-body hydrodynamics in the presence of thermal fluctuations and agree quantitatively with observations. We demonstrate that filament dynamics in this system are primarily governed by a dimensionless elasto-viscous number comparing viscous drag forces to elastic bending forces, with thermal fluctuations playing only a secondary role. While short and rigid filaments perform quasi-periodic tumbling motions, a buckling instability arises above a critical flow strength. A second transition to strongly deformed shapes occurs at a yet larger value of the elasto-viscous number and is characterized by the appearance of localized high-curvature bends that propagate along the filaments in apparent "snaking" motions. A theoretical model for the as yet unexplored onset of snaking accurately predicts the transition and explains the observed dynamics. We present a complete characterization of filament morphologies and transitions as a function of elasto-viscous number and scaled persistence length and demonstrate excellent agreement between theory, experiments, and simulations.

fluid structure interactions | flexible fibers | buckling instabilities | actin filaments

The dynamics and conformational transitions of elastic filaments and semiflexible polymers in viscous fluids underlie the complex non-Newtonian behavior of their suspensions (1) and also play a role in many small-scale biophysical processes from ciliary and flagellar propulsion (2, 3) to intracellular streaming (4, 5). The striking rheological properties of polymer solutions hinge on the microscopic dynamics of individual polymers and particularly on their rotation, stretching, and deformation under flow in the presence of thermal fluctuations. Examples of these dynamics include the coil–stretch (6, 7) and stretch–coil (8, 9) transitions in pure straining flows and the quasi-periodic tumbling and stretching of elastic fibers and polymers in shear flows (10, 11). Elucidating the physics behind these microstructural instabilities and transitions is key to unraveling the mechanisms for their complex rheological behaviors (12), from shear thinning and normal stress differences (13) to viscoelastic instabilities (14) and turbulence (15).

The case of long-chain polymers such as DNA (16), for which the persistence length ℓ_p is much smaller than the contour length L, has been characterized extensively in experiments (7, 17) as well as numerical simulations (18) and mean-field models (19). The dynamics in this case are governed by the competition between thermal entropic forces favoring coiled configurations and viscous stresses that tend to stretch the polymer in strain-dominated flows. The interplay between these two effects is responsible for the coil–stretch transition in elongational flows and tumbling and stretching motions in shear flows, both of which are well captured by classic entropic bead-spring models (20–22).

On the contrary, the dynamics of shorter polymers such as actin filaments (23), for which $L \sim \ell_p$, have been much less investigated and are still not fully understood. Here, it is the subtle interplay of bending forces, thermal fluctuations, and internal tension under viscous loading that instead dictates the dynamics. Indeed, bending energy and thermal fluctuations are now of comparable magnitudes, while the energy associated with stretching is typically much larger due to the small diameter of the molecular filaments (1). This distinguishes these filaments from long entropy-dominated polymers such as DNA in which chain bending plays little role.

The classical case of a rigid rod-like particle in a linear flow has been well understood since the work of Jeffery (24), who first described the periodic tumbling now known as Jeffery orbits occurring in shear flow. When flexibility becomes significant, viscous stresses applied on the filament can overcome bending resistance and lead to structural instabilities reminiscent of Euler buckling of elastic beams (8–10, 25–28). On the other hand, Brownian orientational diffusion has been shown to control the

Significance

Elastic filaments and semiflexible polymers occur ubiquitously in biophysical systems and are key components of many complex fluids, yet our understanding of their conformational dynamics under flow is incomplete. Here, we report on experimental observations of actin filaments in simple shear and characterize their various dynamical regimes from tumbling to buckling and snaking. Numerical simulations accounting for elastohydrodynamics as well as Brownian fluctuations show perfect agreement with measurements. Using a reduced-order theoretical model, we elucidate the unexplained mechanism for the transition to snaking. Our results pave the way for a better understanding of biophysical processes, as well as the rheology of sheared soft materials, and provide a theoretical framework for the exploration of the dynamics of dilute and semidilute suspensions.

Author contributions: Y.L., B.C., D.S., A.L., and O.d.R. designed research; Y.L., A.L., and O.d.R. performed experiments; B.C. and D.S. performed simulations; Y.L., B.C., D.S., A.L., and O.d.R. analyzed data and contributed to the theoretical model; and Y.L., B.C., D.S., A.L., and O.d.R. wrote the paper.

The authors declare no conflict of interest.

This article is a PNAS Direct Submission.

[1]Y.L. and B.C. contributed equally to this work.

[2]To whom correspondence should be addressed. Email: anke.lindner@espci.fr.

This article contains supporting information online at www.pnas.org/lookup/suppl/doi:10.1073/pnas.1805399115/-/DCSupplemental.

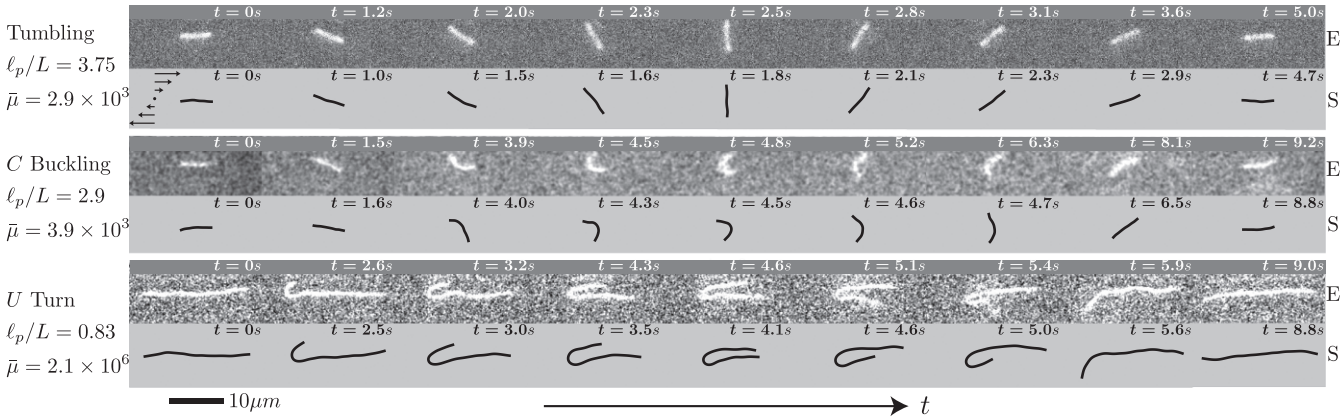

Fig. 1. Temporal evolution of the filament shape in planar shear over one period of motion, showing three representative cases corresponding to increasing elasto-viscous numbers. In each case, we compare fluorescence images from experiments (E) to Brownian dynamics simulations (S). Movies of the dynamics are provided in *SI Appendix*, Movies S1–S6.

characteristic period of tumbling (23, 29). In shear flow, the combination of rotation and deformation leads to particularly rich dynamics (23, 30–35), which have yet to be fully characterized and understood.

In this work, we elucidate these dynamics in a simple shear flow by combining numerical simulations, theoretical modeling, and model experiments using actin filaments. The filaments we consider here have a contour length L in the range of $4-40\,\mu$m and a diameter of $d \sim 8$ nm. By analyzing the fluctuating shapes of the filaments, we measured the persistence length, as shown in ref. 36, to be $\ell_p = 17 \pm 1\,\mu$m independent of the solvent viscosity. We combine fluorescent labeling techniques, microfluidic flow devices, and an automated-stage microscopy apparatus to systematically identify deformation modes and conformational transitions. Our experimental results are compared against Brownian dynamics simulations and theoretical models that describe actin filaments as thermal inextensible Euler–Bernoulli beams whose hydrodynamics follow slender-body theory (10). By varying contour length as well as applied shear rates in the range of $\dot{\gamma} \sim 0.5-10\ \mathrm{s}^{-1}$, we identify and characterize transitions from Jeffery-like tumbling dynamics of stiff filaments to buckled and finally strongly bent configurations for longer filaments.

Results and Discussion

Governing Parameters and Filament Dynamics. In this problem, the filament dynamics result from the interplay of three physical effects—elastic bending forces, thermal fluctuations, and viscous stresses—and are governed by three independent dimensionless groups. First, the ratio of the filament persistence length ℓ_p to the contour length L characterizes the amplitude of transverse fluctuations due to thermal motion, with the limit of $\ell_p/L \to \infty$ describing rigid Brownian fibers. Second, the elasto-viscous number $\bar{\mu}$ compares the characteristic timescale for elastic relaxation of a bending mode to the timescale of the imposed flow and is defined in terms of the solvent viscosity μ, applied shear rate $\dot{\gamma}$, filament length L, and bending rigidity B as $\bar{\mu} = 8\pi\mu\dot{\gamma}L^4/B$. Note that B and ℓ_p are related as $B = k_B T \ell_p$, where k_B is the Boltzmann constant and T the temperature. Third, the anisotropic drag coefficients along the filament involve a geometric parameter $c = -\ln(\epsilon^2 \mathrm{e})$ capturing the effect of slenderness, where $\epsilon = d/L$.

The elasto-viscous number can be viewed as a dimensionless measure of flow strength and exhibits a strong dependence on contour length. By varying L and $\dot{\gamma}$, we have systematically explored filament dynamics over several decades of $\bar{\mu}$ and observed a variety of filament configurations, the most frequent of which we illustrate in Fig. 1 and *SI Appendix*, Movies S1–S6. In relatively weak flows, the filaments are found to tumble without any significant deformation in a manner similar to that of rigid Brownian rods. On increasing the elasto-viscous number, a first transition is observed whereby compressive viscous forces overcome bending rigidity and drive a structural instability toward a characteristic C-shaped configuration during the tumbling motion. By analogy with Euler beams, we term this deformation mode "global buckling" as it occurs over the full length of the filament. In stronger flows, this instability gives way to highly bent configurations, which we call U turns, and they are akin to the snaking motions previously observed with flexible fibers (23, 32). During those turns, the filament remains roughly aligned with the flow direction while a curvature wave initiates at one end and propagates toward the other end. At yet higher values of $\bar{\mu}$, more complex shapes can also emerge, including an S turn which is similar to the U turn but involves two opposing curvature waves emanating simultaneously from both ends (*SI Appendix*, Movies S5 and S6). In all cases, excellent agreement is observed between experimental measurements and Brownian dynamics simulations. Our focus here is in describing and explaining the first three deformation modes and corresponding transitions.

We characterize the temporal shape evolution more quantitatively for each case in Fig. 2. To describe the overall shape and orientation of the filament, we introduce the gyration tensor, or the second mass moment, as

$$G_{ij}(t) = \frac{1}{L}\int_0^L [r_i(s,t) - \bar{r}_i(t)][r_j(s,t) - \bar{r}_j(t)]\, ds, \qquad [1]$$

where $\boldsymbol{r}(s,t)$ is a 2D parametric representation of the filament centerline with arclength $s \in [0, L]$ in the flow-gradient plane, and $\bar{\boldsymbol{r}}(t)$ is the instantaneous center-of-mass position. The angle χ between the mean filament orientation and the flow direction is provided by the eigenvectors of G_{ij}, while its eigenvalues (λ_1, λ_2) can be combined to define a sphericity parameter $\omega = 1 - 4\lambda_1\lambda_2/(\lambda_1 + \lambda_2)^2$ quantifying filament anisotropy: $\omega \approx 0$ for nearly isotropic configurations ($\lambda_1 \approx \lambda_2$), and $\omega \approx 1$ for nearly straight shapes ($\lambda_1 \gg \lambda_2 \approx 0$). Other relevant measures of filament conformation are the scaled end-to-end distance $L_{ee}(t)/L = |\boldsymbol{r}(L,t) - \boldsymbol{r}(0,t)|/L$, whose departures from its maximum value of 1 are indicative of bent or folded shapes, and the total bending energy $E(t) = \frac{B}{2}\int_0^L \kappa^2(s,t)ds$, which is an integrated measure of the filament curvature $\kappa(s,t)$.

As is evident in Fig. 2, these different variables exhibit distinctive signatures in each of the three regimes and can be used to systematically differentiate between configurations.

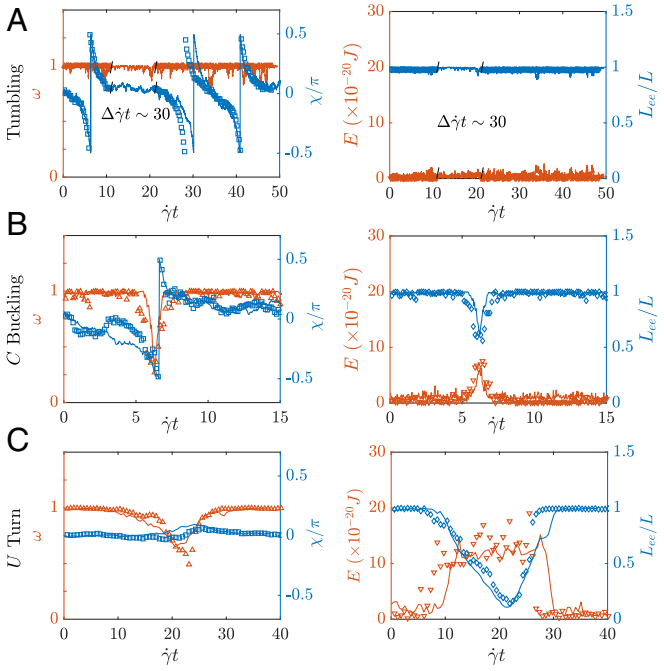

Fig. 2. (*A*–*C*) Evolution of the sphericity parameter ω, mean angle χ with respect to the flow direction, bending energy *E*, and scaled end-to-end distance L_{ee}/L over one period of motion for (*A*) Jeffery-like tumbling, (*B*) *C* buckling, and (*C*) *U* turn. Symbols show experiments. Solid lines are simulations. Parameter values are the same as in Fig. 1. The lack of experimental data during the interval $\Delta\dot{\gamma}t \sim 30$ in *A* is due to a temporary loss of focus caused by tumbling of the filament out of the flow-gradient plane.

During Jeffery-like tumbling, filaments remain nearly straight with $\omega \approx 1$, $L_{ee} \approx L$ and $E \approx 0$ while the angle χ quasi-periodically varies from $-\pi/2$ to $\pi/2$ over the course of each tumble. During a C-buckling event, the angle χ still reaches $\pi/2$, but the other quantities now deviate from their baseline as the filament bends and straightens again. This provides a quantitative measure for distinguishing tumbling motion and C buckling. During a U turn, however, deformations are also significant but χ only weakly deviates from 0 as the filament remains roughly aligned with the flow direction and executes a tank-treading motion rather than an actual tumble. This feature provides a simple test for distinguishing C and U turns in both experiments and simulations. Other hallmarks of U turns are the increased bending energy during the turn, which exhibits a nearly constant plateau while the localized bend in the filament shape travels from one end to the other, and a strong minimum in the end-to-end distance $L_{ee}(t)$, which reaches nearly zero halfway through the turn when the filament is symmetrically folded.

Order Parameters. This descriptive understanding of the dynamics allows us to investigate transitions between deformation regimes as the elasto-viscous number increases. The dependence on $\bar{\mu}$ of the maximum bending energy E, minimum value of the sphericity parameter ω, and range $\Delta\chi$ of the mean angle over one or several periods of motion is shown in Fig. 3. In the case of U turns, the maximum bending energy is calculated as an average over the plateau seen in Fig. 2*C*. In the tumbling regime, deformations are negligible beyond those induced by thermal fluctuations, as evidenced by the nearly constant values of $\max(E) \approx 0$ and $\min(\omega) \approx 1$. After the onset of buckling, however, the maximum bending energy starts increasing monotonically with $\bar{\mu}$ as viscous stresses cause increasingly stronger bending of the filament. This increased bending is accompanied by a decrease in ω as bending renders shapes increasingly isotropic, finally reaching $\min(\omega) \approx 0$. Interestingly, the transition to U turns is marked by a plateau of the bending energy, which subsequently only very weakly increases with $\bar{\mu}$. This plateau is indicative of the emergence of strongly bent configurations, where the elastic energy becomes localized in one sharp fold, and suggests that the curvature of the folds during U turns depends only weakly on flow strength. The parameter ω also starts increasing again after the onset of U turns, as the filaments adopt hairpin shapes that become increasingly anisotropic. Fig. 3 *A* and *B* also shows a few data points for S turns at high values of $\bar{\mu}$: In this regime, the maximum bending energy is approximately twice that of U turns, as bending deformations now become localized in two sharp folds instead of one. S shapes are, however, more compact than U shapes and thus show lower values of ω.

Orientational dynamics are summarized in Fig. 3*C*, showing the range $\Delta\chi = \chi_{\max} - \chi_{\min}$ of the mean angle χ over one period of motion. During a typical Jeffery-like tumbling or C-buckling event, the main filament orientation rotates continuously and as a result $\Delta\chi = \pi$. The scatter in the experimental data is the result of the finite sampling rate during imaging. During U turns, the filament no longer performs tumbles but instead remains globally aligned with the flow direction as it undergoes its snaking motion, resulting in $\Delta\chi < \pi$. This explains the discontinuity in the data of Fig. 3*C*, where C and U turns stand apart. As $\bar{\mu}$ increases beyond the transition, we find that $\Delta\chi \to 0$, suggesting a nearly constant mean orientation for the folded shapes characteristic of U turns.

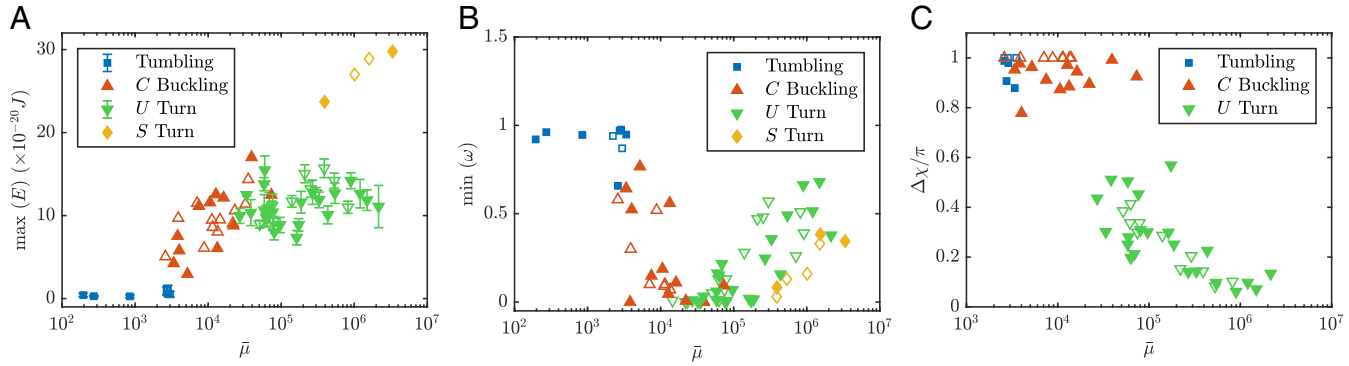

Fig. 3. (*A*–*C*) Dependence on elasto-viscous number $\bar{\mu}$ of (*A*) the maximum value of the bending energy *E*, (*B*) the minimum value of the sphericity parameter ω, and (*C*) the range $\Delta\chi$ of the mean angle in the various tumbling and deformation regimes. Solid symbols show experiments; open symbols show simulations. For experimental data, the measurement error in $\bar{\mu}$ [due to errors in contour length (± 0.5 μm) and in local shear rate (± 0.1 s^{-1})] is comparable to the marker size.

While we have not studied the tumbling frequency extensively, data based on a limited number of simulations and experiments recover the classical 2/3 scaling of frequency on flow strength (21, 23) for the explored range of parameters, with a systematic deviation toward 3/4 in strong flows in agreement with results from Lang et al. (29).

Transitions Between Regimes and Phase Diagram. Our experiments and simulations have uncovered three dynamical regimes with increasing values of $\bar{\mu}$, the transitions between which we now proceed to explain. A summary of our results is provided in Fig. 4 as a phase diagram in the $(\bar{\mu}/c, \ell_p/L)$ parameter space, where the transitions are found to occur at fixed values of $\bar{\mu}/c$ independent of ℓ_p/L. The first transition from tumbling motion to C buckling has received much attention in the past, primarily in the case of non-Brownian filaments (10, 13, 31). This limit is amenable to a linear stability analysis (13), which predicts a supercritical pitchfork bifurcation whereby compressive viscous stresses exerted along the filament as it rotates into the compressional quadrant of the flow are sufficiently strong to induce buckling. The stability analysis is based on local slender-body theory, where the natural control parameter arises as $\bar{\mu}/c$, and predicts buckling above a critical value of $\bar{\mu}_c^{(1)}/c \approx 306.4$ (13), in reasonable agreement with our measurements (Fig. 4).

Thermal fluctuations do not significantly alter this threshold, but instead result in a blurred transition (9, 26, 37) with an increasingly broad transitional regime where both tumbling and C buckling can be observed for a given value of $\bar{\mu}$. When Brownian fluctuations are strong, i.e., for low values of ℓ_p/L, it becomes challenging to differentiate deformations caused by viscous buckling vs. fluctuations, and thus the distinction between the two regimes becomes irrelevant.

Upon increasing $\bar{\mu}/c$, the second conformational transition from C-shaped filaments to elongated hairpin-like U turns undergoing snaking motions occurs. The appearance of U turns (shown in green in Fig. 4) occurs above a critical value $\bar{\mu}_c^{(2)}/c$ that is again largely independent of ℓ_p/L. However, the transition is not sharp, and near the critical value both shapes can be observed simultaneously (indicated by gray symbols in Fig. 4). In fact, a single filament in the transitional regime will typically execute both types of turns, switching stochastically between them

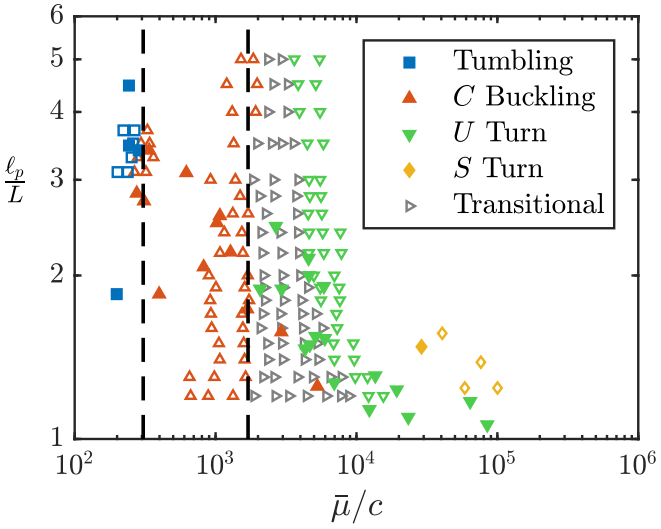

Fig. 4. Phase chart indicating the different dynamical regimes in the $(\bar{\mu}/c, \ell_p/L)$ parameter space. The dashed black lines show the theoretical transitions from tumbling motion to *C* buckling ($\bar{\mu}_c^{(1)}/c \approx 306.4$) and from *C* buckling to *U* turns ($\bar{\mu}_c^{(2)}/c \approx 1{,}700$). Solid symbols show experiments; open symbols show simulations.

(*SI Appendix*, Fig. S6). This transition toward snaking dynamics has not previously been characterized. Our attempt at understanding its mechanism focuses on the onset of a U turn, which always involves the formation of a J-shaped configuration as visible in Fig. 1 and also illustrated in Fig. 5.

To elucidate the transition mechanism, we develop a theoretical model for a J configuration, which can be viewed as a precursor to the U turn. We neglect Brownian fluctuations and idealize the J shape as a semicircle of radius R connected to a straight arm forming an angle ϕ with the flow direction, with both sections undergoing a snaking motion responsible for the U turn; details of the model, which draws on analogies with the tank-treading motion of vesicles (38, 39), can be found in *SI Appendix*, *Theoretical Model*. By satisfying filament inextensibility as well as force and torque balances, and by balancing viscous dissipation in the fluid with the work of elastic forces, we are able to solve for model parameters such as R and ϕ without any fitting. A key aspect of the model is that consistent solutions for these parameters can be obtained only above a critical elasto-viscous number, and this solvability criterion thus provides a threshold $\bar{\mu}_c^{(2)}/c \approx 1{,}700$ below which the J shape ceases to exist. This theoretical prediction is depicted by the dashed line in the phase chart of Fig. 4 and coincides perfectly with the onset of the transitional regime in simulations and experiments.

We can now discuss the initiation of the J shape, in which two possible mechanisms may be at play. On the one hand, it may be caused by the global buckling of the filament in the presence of highly compressive viscous forces, in a manner consistent with the sequence of shapes in Fig. 5*A*. Under sufficiently strong shear, compressive forces can induce a buckling instability on a filament that has not yet aligned with the compressional axis and forms only a small angle with the flow direction. Alignment of the deformed filament with the flow then results in differential tension (compression vs. tension) near its two ends, thus allowing one end to bend while the other remains straight. A second potential mechanism proposed in ref. 29 is of a local buckling occurring on the typical length scale of transverse thermal fluctuations. Our data, however, clearly show that the transition to U turns is independent of thermal fluctuations, allowing us to discard this hypothesis. Thermal fluctuations are nonetheless responsible for the existence of the transitional regime above $\bar{\mu}_c^{(2)}/c$, where they can destabilize J shapes toward C shapes and thus prevent the occurrence of U turns. This interpretation is consistent with the increasing extent of the transitional regime with decreasing ℓ_p/L.

Dynamics of *U* Turns. We further characterize the dynamics during U turns, for which our theoretical model also provides predictions. The filament orientation at the onset of a turn is plotted in Fig. 6*A*, showing the tilt angle ϕ formed by the straight arm of the J shape with respect to the flow direction as a function of $\bar{\mu}$. Our theoretical model for dynamics of the J shape also provides the value of ϕ, in excellent agreement with experiments. In both cases, the tilt angle decreases with increasing flow strength due to increased alignment by the flow. For very long filaments (limit of large $\bar{\mu}$), accurate measurements of the tilt angle become challenging due to shape fluctuations and hence the increased scatter in the data.

After a J shape is initiated as discussed above, the curvature of the folded region remains nearly constant in time as suggested by the plateau in the bending energy (Fig. 3*C*). This provides a strong basis for approximating the bent part of the filament as a semicircle of radius R in our model. The theoretical prediction R_{th} and measurements of the radius on J shapes from experiments and simulations agree quite well in Fig. 6*B* (see *SI Appendix*, Fig. S5 for details). The radius of the bend is seen to

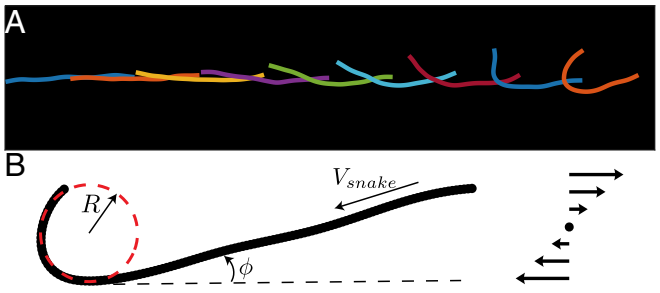

Fig. 5. (*A*) Numerical snapshots of filament shapes during the formation of a *J* shape before the initiation of a *U* turn. (*B*) The *J* shape can be approximated by a semicircle of radius *R* connected to a straight arm forming a tilt angle of ϕ with the flow direction. During snaking, the filament translates tangentially with an axial velocity V_{snake}.

decrease with $\bar{\mu}$, as compressive viscous stresses in strong flows allow increasingly tighter folding of the filament.

The rotation of the end-to-end vector during the U turn results primarily from tank treading of the filament along its arclength, unlike the global rotation that dominates the tumbling and C-buckling regimes. While the snaking velocity is not constant during a turn, its average value can be quantitatively measured through the time derivative of the end-to-end distance, yielding the approximation $V_{snake} \approx \dot{L}_{ee}/2$. The relevant dynamic length scales and timescales during this snaking motion are the radius of curvature R of the bent segment and shear rate $\dot{\gamma}$. This is supported by our theory, where rescaling V_{snake} by $\dot{\gamma}R_{th}$ collapses the predicted velocities over a range of filament lengths (*SI Appendix*, Fig. S3). The same rescaling applied to the experimental and numerical data and using the theoretical radius R_{th} also provides a good collapse in Fig. 6*C*.

Harasim et al. (23) previously proposed a simplified theory of the U turn, which shares similarities with ours but assumes that the filament is aligned with the flow direction and neglects elastic stresses inside the fold. Their predictions are in partial agreement with our results in the limit of very long filaments and strong shear (*SI Appendix*, *Theoretical Model*). Their theory is unable to predict and explain the transition from buckling to U turns.

Concluding Remarks. Using stabilized actin filaments as a model polymer, we have systematically studied and analyzed the conformational transitions of elastic Brownian filaments in simple shear flow as the elasto-viscous number is increased. Our experimental measurements were shown to be in excellent agreement with a computational model describing the filaments as fluctuating elastic rods with slender-body hydrodynamics. By varying filament contour length and applied shear rate, we performed a broad exploration of the parameter space and confirmed the existence of a sequence of transitions, from rod-like tumbling to elastic buckling to snaking motions. While snaking motions had been previously observed in a number of experimental configurations, the existence of a C-buckling regime had not been confirmed clearly. This is due to the fact that C buckling is visible over only a limited range of elasto-viscous numbers and occurs only in simple shear flow, which is challenging to realize experimentally. We showed that both transitions are primarily governed by $\bar{\mu}/c$. Brownian fluctuations do not modify the thresholds but tend to blur the transitions by allowing distinct dynamics to coexist over certain ranges of $\bar{\mu}$.

While the first transition from tumbling to buckling had been previously described as a supercritical linear buckling instability (13), the transition from buckling to snaking was heretofore unexplained. Using a simple analytical model for the dynamics of the J shape that is the precursor to snaking turns, we were able to obtain a theoretical prediction for the threshold elasto-viscous number above which snake turns become possible. The model did not take thermal noise into account, but highlighted the subtle role played by tension and compression during the onset of the turn. Our analysis and model lay the groundwork for illuminating a wide range of other complex phenomena in polymer solutions, from their rheological response in flow and dynamics in semidilute solutions (40, 41) to migration under confinement and microfluidic control of filament dynamics.

Materials and Methods

Experimental Methods. The protocol for assembly of the actin filaments is well controlled and reproducible. Concentrated G-actin, which is obtained from rabbit muscle and purified according to the protocol described in ref. 42, is placed into F buffer (10 mM Tris·HCl, pH 7.8, 0.2 mM ATP, 0.2 mM $CaCl_2$, 1 mM DTT, 1 mM $MgCl_2$, 100 mM KCl, 0.2 mM EGTA, and 0.145 mM DABCO) at a final concentration of 1 μM. At the same time, Alexa488-fluorescent phalloidin in the same molarity as G-actin is added to prevent depolymerization and thus to stabilize as well as to visualize the filaments. After 1 h of polymerization in the dark at room temperature, concentrated F-actin is stored at 4 °C for the following experiments. To avoid interactions between filaments, F-actin used in experiments has a final concentration of 0.1 nM obtained by diluting the previous solution with F buffer. A total of 1 mM ascorbic acid is added to decrease photobleaching effects and 45.5% (wt/vol) sucrose to match the refractive index of the polydimethylsiloxane (PDMS) channel ($n = 1.41$). The viscosity of the dilute filament suspension is 5.6 mPa·s at 20 °C, measured on an Anton Paar MCR 501 rheometer.

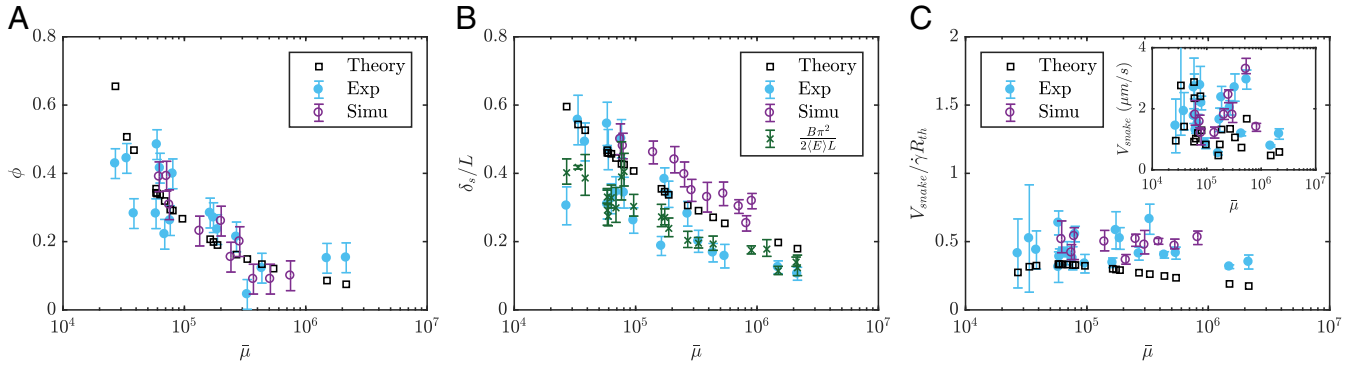

Fig. 6. (*A*) Dependence on $\bar{\mu}$ of the tilt angle ϕ formed by *J* shapes with respect to the flow direction in experiments, in simulations, and in our theoretical model. (*B*) Fraction δ_s/L of the filament length that is bent during a *U* turn (see *SI Appendix*, Fig. S4 for the detailed definition of δ_s). The theoretical predictions are based on the *J* shape at the start of the turn. Since the bending energy during a *U* turn is concentrated in the fold, an estimate for δ_s/L is also provided by $B\pi^2/2\langle E\rangle L$, where $\langle E\rangle$ is the average bending energy during the turn, and good agreement is found between both measures. (*C*) Snaking velocity V_{snake} rescaled with $\dot{\gamma}R_{th}$ and plotted against $\bar{\mu}$ from experiments, simulations, and theory; here, R_{th} is the theoretically predicted fold radius.

A micro-PDMS channel is designed as a vertical Hele–Shaw cell, with length $L = 30$ mm, height $H = 500\ \mu$m, and width $W = 150\ \mu$m. In this geometry the filament dynamics can be directly observed in the horizontal shear plane whereas shear in the vertical direction can be neglected at a sufficient distance from the bottom wall (see *SI Appendix, Microuidic Channel Geometry* for more details). To consider pure shear flow, filament and flow scales should be properly separated, and we thus chose a width (150 μm) much larger than the typical dimension of the deformed filament ($\approx$10μm). An objective with long working distance is required to observe in a plane far enough from the bottom; the objective should also have a large numerical aperture to collect as much light as possible from the fluorescent actin filaments. To combine both of these requirements, we used a water immersion objective from Zeiss (63$\times$ C-Apochromat /1.2 N.A.) with working distance $\approx 280\ \mu$m.

Stable flow is driven by a syringe pump (Cellix ExiGo) and particle-tracking velocimetry is used to check the agreement of the velocity profile with theoretical predictions (43). We impose flow rates Q in the range of 5$-$7.5 nL/s, leading to typical filament velocities $u_x \sim 20-150\ \mu$m/s in the observation area in the plane $z = 150\ \mu$m. The filament Reynolds number is of the order $\mathrm{Re} \sim 10^{-4}$. To follow the filaments during their transport in the channel we use a motorized stage programmed to accurately follow the flow and also to correct for small changes in the z plane, occurring due to slight bending of the channel. This step is necessary as the focal depth of the objective is only a few micrometers and streamlines need to be followed with high precision over distances of several millimeters.

Images are captured by a s-CMOS camera (HAMAMATSU ORCA flash 4.0LT, 16 bits) with an exposure time of $\Delta t = 65$ ms and are synchronized with the stage displacement. They are processed by Image J to obtain the position of the center of mass and the filament shape. The center of mass is used to calculate the local shear rate experienced by the filament. The shape is extracted through Gaussian blur, threshold, noise reduction, and skeletonize procedures. A custom MATLAB code is then used to reconstruct the filament centerline as a sequence of discrete points along the arclength s and to calculate the parameters plotted in Fig. 2.

Modeling and Simulations. We model the filaments as inextensible Euler–Bernoulli beams and use nonlocal slender-body hydrodynamics to capture drag anisotropy and hydrodynamic interactions (10, 25). Simulations without hydrodynamic interactions (free-draining model) were also performed but did not compare well with experiments. Brownian fluctuations are included and satisfy the fluctuation–dissipation theorem. As experiments consider only quasi-2D trajectories involving dynamics in the focal plane, we perform all simulations in 2D and indeed found better agreement compared with 3D simulations. Details of the governing equations and numerical methods are provided in *SI Appendix, Computational Model and Methods*. The simulation code is available upon request to the authors.

ACKNOWLEDGMENTS. We are grateful to Guillaume Romet-Lemonne and Antoine Jégou for providing purified actin and to Thierry Darnige for help with the programming of the microscope stage. We thank Michael Shelley, Lisa Fauci, Julien Deschamps, Andreas Bausch, Gwenn Boedec, Anupam Pandey, Harishankar Manikantan, and Lailai Zhu for useful discussions and Roberto Alonso-Matilla for checking some of our calculations. The authors acknowledge support from European Research Council Consolidator Grant 682367, from a Chinese Scholarship Council Scholarship, and from NSF Grant CBET-1532652.

1. Lindner A, Shelley M (2016) Elastic fibers in flows. *Fluid-Structure Interactions in Low-Reynolds-Number Flows* (The Royal Society of Chemistry, Cambridge, UK), pp 168–192.
2. Brennen C, Winet H (1977) Fluid mechanics of propulsion by cilia and flagella. *Annu Rev Fluid Mech* 9:339–398.
3. Blake JR (2001) Fluid mechanics of ciliary propulsion. *Computational Modeling in Biological Fluid Dynamics* eds Fauci L, Gueron S (Springer, New York), pp 1–51.
4. Ganguly S, Williams LS, Palacios IM, Goldstein RE (2012) Cytoplasmic streaming in Drosophila oocytes varies with kinesin activity and correlates with the microtubule cytoskeleton architecture. *Proc Natl Acad Sci USA* 109:15109–15114.
5. Suzuki K, Miyazaki M, Takagi J, Itabashi T, Ishiwata S (2017) Spatial confinement of active microtubule networks induces large-scale rotational cytoplasmic flow. *Proc Natl Acad Sci USA* 114:2922–2927.
6. De Gennes P (1974) Coil-stretch transition of dilute flexible polymers under ultrahigh velocity gradients. *J Chem Phys* 60:5030–5042.
7. Schroeder CM, Babcock HP, Shaqfeh ES, Chu S (2003) Observation of polymer conformation hysteresis in extensional flow. *Science* 301:1515–1519.
8. Young YN, Shelley MJ (2007) Stretch-coil transition and transport of fibers in cellular flows. *Phys Rev Lett* 99:058303.
9. Kantsler V, Goldstein RE (2012) Fluctuations, dynamics, and the stretch-coil transition of single actin filaments in extensional flows. *Phys Rev Lett* 108: 038103.
10. Tornberg AK, Shelley MJ (2004) Simulating the dynamics and interactions of flexible fibers in Stokes flows. *J Comp Phys* 196:8–40.
11. Schroeder CM, Texeira RE, Shaqfeh ESG, Chu S (2005) Characteristic periodic motion of polymers in shear flow. *Phys Rev Lett* 95:018301.
12. Bird RB, Armstrong RC, Hassager O, Curtiss CF (1977) *Dynamics of Polymeric Liquids* (Wiley, New York), Vol 1.
13. Becker LE, Shelley MJ (2001) Instability of elastic filaments in shear flow yields first-normal-stress differences. *Phys Rev Lett* 87:198301.
14. Shaqfeh ESG (1996) Purely elastic instabilities in viscometric flows. *Annu Rev Fluid Mech* 28:129–185.
15. Morozov AN, van Saarloos W (2007) An introductory essay on subcritical instabilities and the transition to turbulence in visco-elastic parallel shear flows. *Phys Rep* 447:112–143.
16. Schroeder CM (2018) Single polymer dynamics for molecular rheology. *J Rheol* 62:371–403.
17. Perkins TT, Smith DE, Chu S (1997) Single polymer dynamics in an elongational flow. *Science* 276:2016–2021.
18. Hur JS, Shaqfeh ES, Larson RG (2000) Brownian dynamics simulations of single DNA molecules in shear flow. *J Rheol* 44:713–742.
19. Gerashchenko S, Steinberg V (2006) Statistics of tumbling of a single polymer molecule in shear flow. *Phys Rev Lett* 96:038304.
20. Schroeder CM, Shaqfeh ESG, Chu S (2004) Effect of hydrodynamic interactions on DNA dynamics in extensional flow: Simulation and single molecule experiment. *Macromolecules* 37:9242–9256.
21. Schroeder CM, Teixeira RE, Shaqfeh ES, Chu S (2005) Characteristic periodic motion of polymers in shear flow. *Phys Rev Lett* 95:018301.
22. Hsieh CC, Larson RG (2005) Prediction of coil-stretch hysteresis for dilute polystyrene molecules in extensional flow. *J Rheol* 49:1081–1089.
23. Harasim M, Wunderlich B, Peleg O, Kröger M, Bausch AR (2013) Direct observation of the dynamics of semiflexible polymers in shear flow. *Phys Rev Lett* 110:108302.
24. Jeffery GB (1922) The motion of ellipsoidal particles immersed in a viscous fluid. *Proc R Soc Lond A* 102:161–179.
25. Manikantan H, Saintillan D (2013) Subdiffusive transport of fluctuating elastic filaments in cellular flows. *Phys Fluids* 25:073603.
26. Manikantan H, Saintillan D (2015) Buckling transition of a semiflexible filament in extensional flow. *Phys Rev E* 92:041002.
27. Quennouz N, Shelley M, du Roure O, Lindner A (2015) Transport and buckling dynamics of an elastic fibre in a viscous cellular flow. *J Fluid Mech* 769:387–402.
28. Guglielmini L, Kushwaha A, Shaqfeh E, Stone H (2012) Buckling transitions of an elastic filament in a viscous stagnation point flow. *Phys Fluids* 24:123601.
29. Lang PS, Obermayer B, Frey E (2014) Dynamics of a semiflexible polymer or polymer ring in shear flow. *Phys Rev E* 89:022606.
30. Munk T, Hallatschek O, Wiggins CH, Frey E (2006) Dynamics of semiflexible polymers in a flow field. *Phys Rev E* 74:041911.
31. Nguyen H, Fauci L (2014) Hydrodynamics of diatom chains and semiflexible fibres. *J R Soc Interface* 11:20140314.
32. Forgacs O, Mason S (1959) Particle motions in sheared suspensions: X. Orbits of flexible threadlike particles. *J Colloid Sci* 14:473–491.
33. Pawłowska S, et al. (2017) Lateral migration of electrospun hydrogel nanofilaments in an oscillatory flow. *PLoS One* 12:1–21.
34. Delmotte B, Climent E, Plouraboué F (2015) A general formulation of Bead Models applied to flexible fibers and active filaments at low Reynolds number. *J Comput Phys* 286:14–37.
35. Chelakkot R, Winkler RG, Gompper G (2010) Migration of semiflexible polymers in microcapillary flow. *Europhys Lett* 91:14001.
36. Gittes F, Mickey B, Nettleton J, Howard J (1993) Flexural rigidity of microtubules and actin filaments measured from thermal fluctuations in shape. *J Cell Biol* 120: 923.
37. Baczynski K, Lipowsky R, Kierfeld J (2007) Stretching of buckled filaments by thermal fluctuations. *Phys Rev E* 76:061914.
38. Keller SR, Skalak R (1982) Motion of a tank-treading ellipsoidal particle in a shear flow. *J Fluid Mech* 120:27–47.
39. Rioual F, Biben T, Misbah C (2004) Analytical analysis of a vesicle tumbling under a shear flow. *Phys Rev E* 69:061914.
40. Kirchenbuechler I, Guu D, Kurniawan Na, Koenderink GH, Lettinga MP (2014) Direct visualization of flow-induced conformational transitions of single actin filaments in entangled solutions. *Nat Commun* 5:5060.
41. Huber B, Harasim M, Wunderlich B, Kröger M, Bausch AR (2014) Microscopic origin of the non-Newtonian viscosity of semiflexible polymer solutions in the semidilute regime. *ACS Macro Lett* 3:136–140.
42. Spudich JA, Watt S (1971) The regulation of rabbit skeletal muscle contraction I. Biochemical studies of the interaction of the tropomyosin-troponin complex with actin and the proteolytic fragments of myosin. *J Biol Chem* 246:4866–4871.
43. White FM, Corfield I (2006) *Viscous Fluid Flow* (McGraw-Hill, New York), Vol 3.